PAPER

Inducing preferential growth of the Zn (002) plane by using a multifunctional chelator for achieving highly reversible Zn anodes†

Xi Li,[a] Zhenjie Chen, [ID][a] Pengchao Ruan,[b] Xueting Hu,[b] Bingan Lu, [ID][c] Xiaoming Yuan, [ID][d] Siyu Tian*[b,e] and Jiang Zhou [ID] *[b]

Aqueous zinc-ion batteries (AZIBs) have demonstrated great potential for large-scale energy storage. However, their practical applications have been restricted by fast Zn dendrite growth and severe side reactions at the Zn/electrolyte interface. Herein, sodium gluconate is incorporated into a mild acidic electrolyte as a multifunctional additive to stabilize the Zn anode. Experiments and theoretical calculations reveal that the SG additive can induce planar growth of Zn along its (002) direction, thereby inhibiting Zn dendrite growth. This dendrite inhibition effect is attributed to the preferential adsorption of Zn^{2+} on the Zn (002) plane, while the Zn (100) and (101) planes are shielded by gluconate ions. Consequently, Zn||Zn symmetric cells with the electrolyte additive exhibit significantly prolonged cycle lives of 2000 h at 1 mA cm^{-2}, 1 mA h cm^{-2} and 900 h at 5 mA cm^{-2}, 2.5 mA h cm^{-2}. Futhermore, the Zn||$NH_4V_4O_{10}$ full cell retains 95% of its initial capacity after 2000 cycles at a current density of 5 A g^{-1} with an average CE of nearly 100%. This work offers a cost-effective strategy to enhance the electrochemical performance of AZIBs.

1. Introduction

The development and utilization of renewable energy systems have garnered growing attention to address the global energy and environmental challenges.[1,2] As one of the key energy storage systems, lithium-ion batteries dominate the current commercial market. However, the scarcity of lithium and the flammability of organic electrolytes raise growing concerns about their sustainability and safety for large-scale applications.[3,4] In comparison, aqueous zinc-ion batteries (AZIBs) have been considered a promising alternative to lithium-ion batteries, owing to their high theoretical capacity (820 mA h g^{-1}), low cost (US\$65 kW h^{-1}), low redox potential

(−0.76 V *vs.* the standard hydrogen electrode), high elemental abundance, excellent safety, and environment friendliness.[5–8] Nonetheless, the development of AZIBs is hindered by rampant Zn dendrite growth and severe water-induced side reactions (*e.g.*, Zn corrosion and byproduct passivation).[2] These detrimental processes result in rapid capacity degradation and quick failure of AZIBs.[9,10]

To overcome these challenges, many strategies have been proposed, including Zn alloying,[11,12] artificial coating,[13,14] separator functionalization,[15,16] and electrolyte engineering.[17–20] Among these strategies, engineering electrolytes using additives is considered an efficient and effective approach to stabilize the Zn anode. For instance, inert cations dissociated from metallic salts can be electrostatically absorbed on the tips of Zn dendrites, forming a shielding layer that facilitates uniform Zn deposition.[21] However, the effectiveness of inert cations is limited due to their non-preferential adsorption on the Zn surface. In contrast, organic molecules have a strong affinity for Zn^{2+} and Zn metal, capable of altering Zn^{2+} solvation structures, suppressing interfacial side reactions, and inhibiting Zn dendrite growth. Additionally, organic molecules have been proved to facilitate preferential Zn deposition along its specific crystal planes.[22] Given the hexagonal close-packed crystal structure of Zn, this alteration of Zn plating/stripping behaviors leads to distinct morphologies of the resulting Zn deposits. For instance, Zn deposition exhibits planar growth behav-

[a]*Hunan Provincial Key Laboratory of Flexible Electronic Materials Genome Engineering, Changsha University of Science and Technology, Changsha 410004, China*
[b]*School of Materials Science and Engineering, Hunan Provincial Key Laboratory of Electronic Packaging and Advanced Functional Materials, Central South University, Changsha 410083, China. E-mail: zhou_jiang@csu.edu.cn*
[c]*School of Physics and Electronics, Hunan University, Changsha 410082, China*
[d]*Hunan Key Laboratory of Nanophotonics and Devices, School of Physics, Central South University, 932 South Lushan Road, Changsha 410083, China*
[e]*Department of Mechanical Engineering, The University of Texas at Dallas, 800 W Campbell Rd, Richardson, Texas 75080, USA. E-mail: siyu.tian@utdallas.edu*
†Electronic supplementary information (ESI) available. See DOI: https://doi.org/10.1039/d3nr05699f
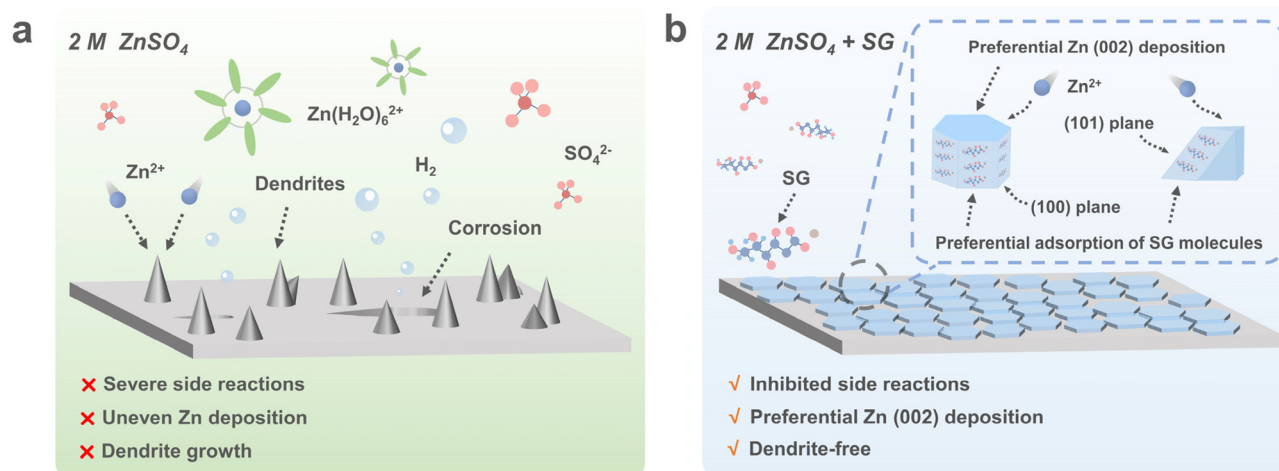
Fig. 1 Schematic illustrations of Zn deposition in different electrolytes: (a) 2 M ZnSO$_4$ and (b) 2 M ZnSO$_4$ in the presence of 20 mM SG molecules. The inset depicts the preferential growth of Zn (002) induced by SG molecules.

ior along the Zn (002) plane, which is beneficial for suppressing dendrite growth and inhibiting water-induced side reactions at the Zn/electrolyte interface.[23] Conversely, Zn deposition along the (100) and (101) planes leads to rapid dendrite growth, causing battery short circuits and accelerating water-induced side reactions.[23-25] Therefore, promoting planar growth along the Zn (002) plane during charge/discharge is highly desired for the development of high-performance AZIBs.

Herein, we introduce a chelating agent, sodium gluconate (SG), as a multifunctional additive in a 2 M ZnSO$_4$ electrolyte to enhance the reversibility of the Zn anode. Without the SG additive, Zn deposition proceeds along its (100) and (101) crystalline planes, leading to rapid dendrite growth and severe side reactions. However, SG molecules with abundant functional groups exhibit strong adsorption energies on the Zn (101) and (100) planes. This facilitates the preferential adsorption of SG molecules and blocks Zn deposition on these planes. Consequently, Zn growth is preferentially guided along the (002) plane, enabling highly reversible and dendrite-free Zn anodes (Fig. 1). Benefiting from the SG additive, Zn||Zn symmetric cells exhibit significantly prolonged cycle lives of 2000 h at 1 mA cm^{-2}, 1 mA h cm^{-2} and 900 h at 5 mA cm^{-2}, 2.5 mA h cm^{-2}. Moreover, 95% of the capacity of the NH$_4$V$_4$O$_{10}$||Zn full cell is retained after 2000 cycles at a current density of 5 A g^{-1}. This work highlights the preferential Zn deposition facilitated by the SG electrolyte additive for achieving highly reversible AZIBs.

2.   Results and discussion

To investigate the influence of the additive on the stability of Zn anodes, different concentrations of SG were added to the 2 M ZnSO$_4$ (ZS) electrolyte. For instance, the electrolytes containing 10, 20, 50, 80 and 100 mM SG were denoted as SG10,

SG20, SG50, SG80 and SG100, respectively. As shown in Fig. 2a, the ZS-based Zn||Zn symmetric cell failed after approximately 500 h at a current density of 1 mA cm^{-2} and an areal capacity of 1 mA h cm^{-2} due to severe side reactions and rapid Zn dendrite growth. In sharp contrast, the cycle life of the SG20-based Zn||Zn symmetric cell was remarkably extended to 2000 h, surpassing those of symmetric cells using electrolytes with other SG concentrations (Fig. S1†). Although the SG80-based Zn||Zn symmetric cell exhibited a similar cycle life, the SG20 electrolyte offered superior cost advantage since less SG additive was used. With a higher SG concentration, the SG100-based symmetric cell failed after 1100 h (Fig. S1†). Therefore, SG20 was selected as the optimal electrolyte for further tests. With the optimal SG20 electrolyte, the Zn||Zn symmetric cell also exhibited excellent cycling stability over 900 h at a high current density of 5 mA cm^{-2} and a high areal capacity of 2.5 mA h cm^{-2} (Fig. 2b). Under such harsh cycling conditions, the ZS-based symmetric cell quickly failed after 200 h due to accelerated Zn dendrite growth under high current density and areal capacity.[7]

The rate capability of the symmetric cells was evaluated at current densities ranging from 1 to 10 mA cm^{-2} with a constant areal capacity of 1 mA h cm^{-2}. As shown in Fig. 2c, the ZS-based symmetric cell exhibited higher overpotentials (*e.g.*, 54 mV at 2 mA cm^{-2}) and failed after only 30 h during the rate tests. Meanwhile, the overpotential of the SG20-based Zn||Zn symmetric cell decreased to 38 mV at 2 mA cm^{-2}, and the cell remained stable at different current densities, indicating enhanced rate performance in the presence of SG additives. Fig. 2d displays the coulombic efficiency (CE) of the Zn||Cu asymmetric cells based on different electrolytes. The ZS-based asymmetric cell failed after 120 cycles, which could be ascribed to detrimental side reactions and "dead Zn" induced by dendrite growth.[6] In comparison, the SG20-based asymmetric cell exhibited an average CE of 98.9% over 150 cycles, outperforming the ZS-based asymmetric cell. Furthermore,
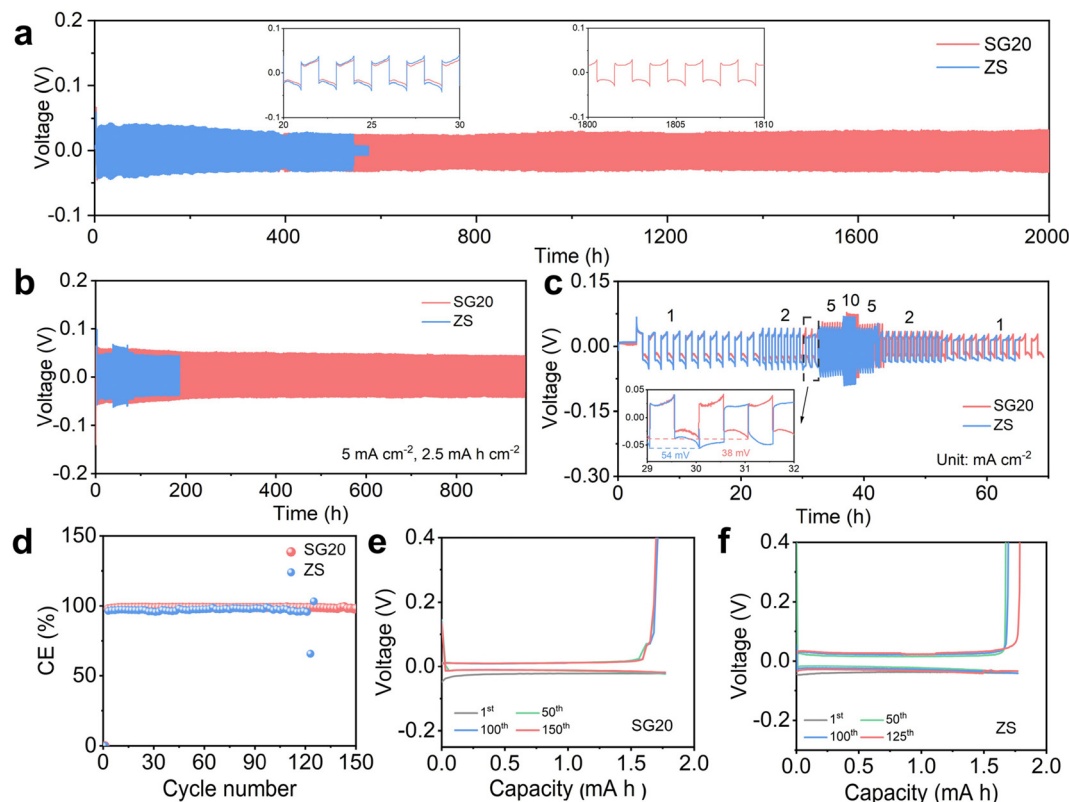
Fig. 2 Long-term cycling performance of Zn||Zn symmetric cells assembled using ZS and SG20 electrolytes at (a) 1 mA cm^{-2} with a capacity of 1 mA h cm^{-2} and (b) 5 mA cm^{-2} with a capacity of 2.5 mA h cm^{-2}. (c) Rate performance of Zn||Zn symmetric cells assembled using ZS and SG20 electrolytes. (d) CEs of Zn||Cu asymmetric cells at 1 mA cm^{-2} with a capacity of 1 mA h cm^{-2}. Voltage profiles of Zn||Cu asymmetric cells at different cycles based on (e) SG20 and (f) ZS electrolytes.

Fig. 2e and f present the voltage profiles of these Zn||Cu asymmetric cells. The SG20-based Zn||Cu asymmetric cell exhibited lower overpotentials (~40 mV) and overlapped voltage profiles, indicating high Zn plating/stripping reversibility. Comparatively, the ZS-based Zn||Cu asymmetric cell showed a high overpotential of approximately 60 mV. These findings validate the effectiveness of the SG additive in enhancing Zn plating/stripping reversibility.

To intuitively present the Zn deposition behavior, an optical microscope was utilized to observe the evolution of the Zn/electrolyte interface during Zn plating with a current density of 10 mA cm^{-2}. As shown in Fig. 3a, the Zn/electrolyte interface became irregular with many protrusions and cavities due to Zn dendrite growth in the ZS electrolyte. In contrast, the Zn/electrolyte interface remained flat in the SG20 electrolyte with a uniform and dense Zn plating layer, indicating that the SG additive effectively facilitated uniform Zn deposition (Fig. 3b). Fig. 3c and d display the scanning electron microscopy (SEM) images of the Zn deposits obtained in ZS and SG20 electrolytes. The Zn deposited in the ZS electrolyte exhibited a disordered and dendritic morphology. In contrast, the Zn deposits obtained in the SG20 electrolyte were more uniform and denser. The cross-sectional SEM images shown in Fig. S2† further confirm the uniform deposition of Zn in the SG20 electrolyte.

Fig. S3 and 4† show the distributions of Zn, O, and S elements on the surface of cycled Zn anodes obtained by energy-dispersive X-ray spectroscopy (EDS). The Zn anode cycled in the SG20 electrolyte exhibited notably lower contents of O and S elements than the Zn anode cycled in the ZS electrolyte. This suggested that water-induced side reactions, particularly the formation of zinc hydroxide sulfate (ZHS) byproducts, were effectively suppressed by the SG additive during Zn plating/stripping.[26] Fig. 3e and Fig. S5† display the X-ray diffraction (XRD) patterns of the Zn anodes cycled in different electrolytes. As shown in Fig. 3e, no ZHS peaks existed in the XRD pattern of the Zn anode cycled in the SG20 electrolyte, agreeing well with the findings of the EDS analysis. Meanwhile, new diffraction peaks corresponding to ZHS byproducts emerged in the XRD patterns of the Zn anodes cycled in ZS and other SG-based electrolytes (Fig. 3e and Fig. S5†) because of water-induced side reactions. Additionally, Fig. 3e shows that the relative intensity of the (002) peak reached its maximum when the Zn anode was cycled in the optimal SG20 electrolyte. In other SG-based (such as SG10, SG50 and SG80) and ZS electrolytes, the relative intensity of the (002) peak decreased, as displayed in Fig. S5.† These results suggest that SG molecules can induce preferential Zn deposition along the (002) direction, inhibiting Zn dendrite growth and suppressing water-induced side reactions. However, excess SG molecules could also miti-
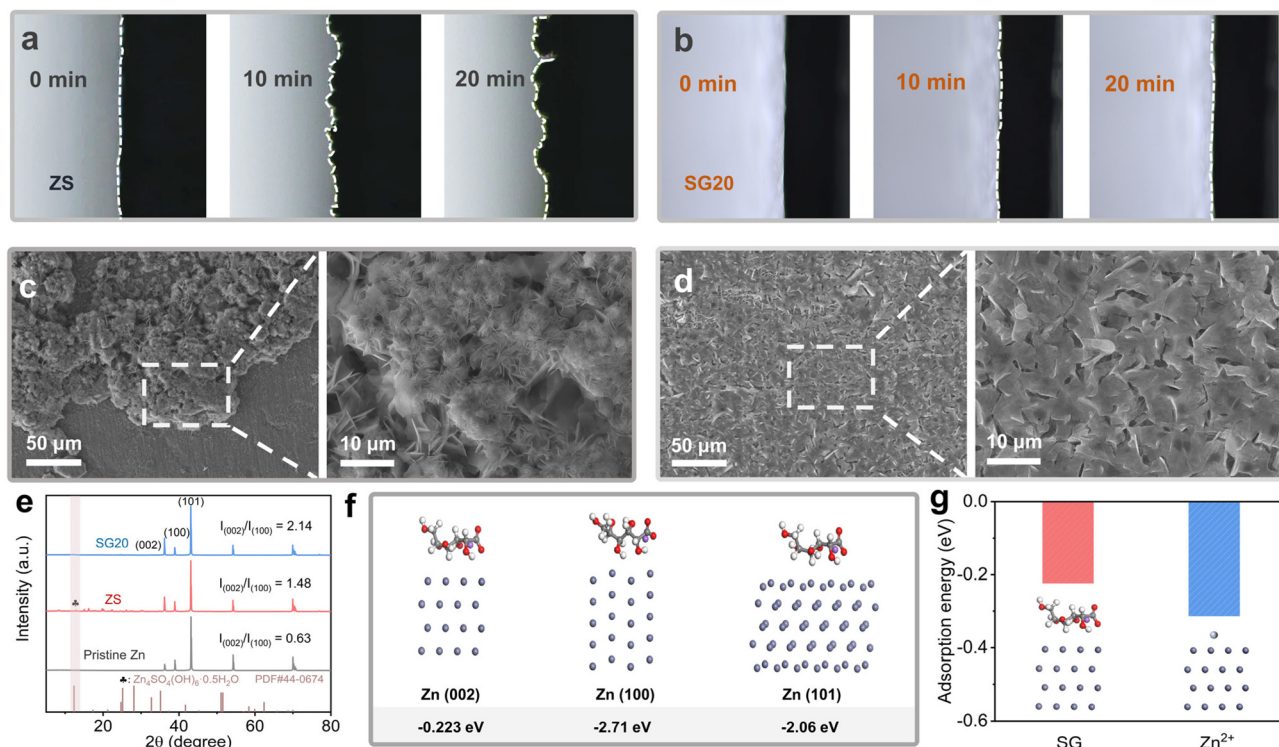
Fig. 3 *In situ* optical images of Zn deposition in (a) ZS and (b) SG20 electrolytes. SEM images of Zn anodes after cycling in (c) ZS and (d) SG20 electrolytes. (e) XRD patterns of pristine Zn and Zn anodes after 50 cycles in SG20 and ZS electrolytes at 1 mA cm^{-2} and 1 mA h cm^{-2}. (f) Adsorption energies of SG molecules on different crystal planes of Zn. (g) Adsorption energies of SG molecules and Zn^{2+} on the Zn (002) plane.

gate their enhancement effects on the reversibility of the Zn anodes.

To understand the fundamental mechanisms associated with SG molecules, density functional theory (DFT) calculations were performed to investigate their adsorption energies on different Zn crystal planes. Three crystal planes, including (100), (101) and (002), were considered due to the hexagonal close-packed structure of Zn (Fig. S6†). As displayed in Fig. 3f, SG molecules exhibited high adsorption energies (E_{ads}) of −2.71 and −2.06 eV on the (100) and (101) planes, respectively. These values markedly exceeded their E_{ads} (−0.22 eV) on the Zn (002) plane, indicating that the adsorption of SG molecules on the (100) and (101) planes was more favorable. Additionally, the E_{ads} of Zn^{2+} adsorption on the (100) plane was lower than that of SG adsorption (Fig. S7†). Therefore, SG molecules could be preferentially adsorbed on the Zn (100) plane prior to Zn^{2+} adsorption in SG-based electrolytes. Meanwhile, the E_{ads} between Zn^{2+} and the Zn (002) plane reached −0.31 eV, noticeably higher than that between SG molecules and the Zn (002) plane (Fig. 3g). This indicates that the Zn (002) plane can be exposed to Zn^{2+} instead of being shielded by SG molecules at an optimal SG concentration, enabling preferential Zn deposition along the (002) direction. In the absence of SG molecules, Zn deposition in the ZS electrolyte occurred across different crystalline planes, resulting in Zn dendrite growth. These findings are in good agreement with the experimental results.

Fig. 4a presents the Zn nucleation overpotentials of the Zn||Cu symmetric cells based on different electrolytes. The SG20-based Zn||Cu cell exhibited a Zn nucleation overpotential of 10.6 mV, lower than that of the ZS-based Zn||Cu cell. This suggested that the formation of Zn nuclei on the (002) plane required less energy than that on other planes, thereby facilitating the preferential Zn deposition along the (002) direction.[23,27,28] Fig. 4b displays the chronoamperometry (CA) tests of the Zn electrodes conducted in different electrolytes at a constant overpotential of −200 mV. The current density of the Zn electrode increased significantly and reached 35 mA cm^{-2} within 300 s in the ZS electrolyte. The rampant increase in current density indicated two-dimensional diffusion of Zn^{2+} and the formation of Zn dendrites.[22,29] In contrast, for the Zn electrode tested in the SG20 electrolyte, the current density stabilized at approximately 18 mA cm^{-2} after 100 s due to the planar Zn deposition modulated by SG molecules. Furthermore, the SG20-based Zn||Zn symmetric cell exhibited a lower charge transfer impedance (R_{ct}) than the ZS-based symmetric cell (Fig. 4c), suggesting fast charge transfer kinetics at the Zn/electrolyte interface in the SG20 electrolyte.

Fig. 4d shows the linear sweep voltammetry (LSV) tests of the Zn electrodes performed in different electrolytes. The onset potential of the hydrogen evolution reaction (HER) significantly shifted from −1.90 V *vs.* Ag/AgCl in the ZS electrolyte to −2.03 V *vs.* Ag/AgCl in the SG20 electrolyte at a current density of 20 mA cm^{-2}. This indicates the effective suppression
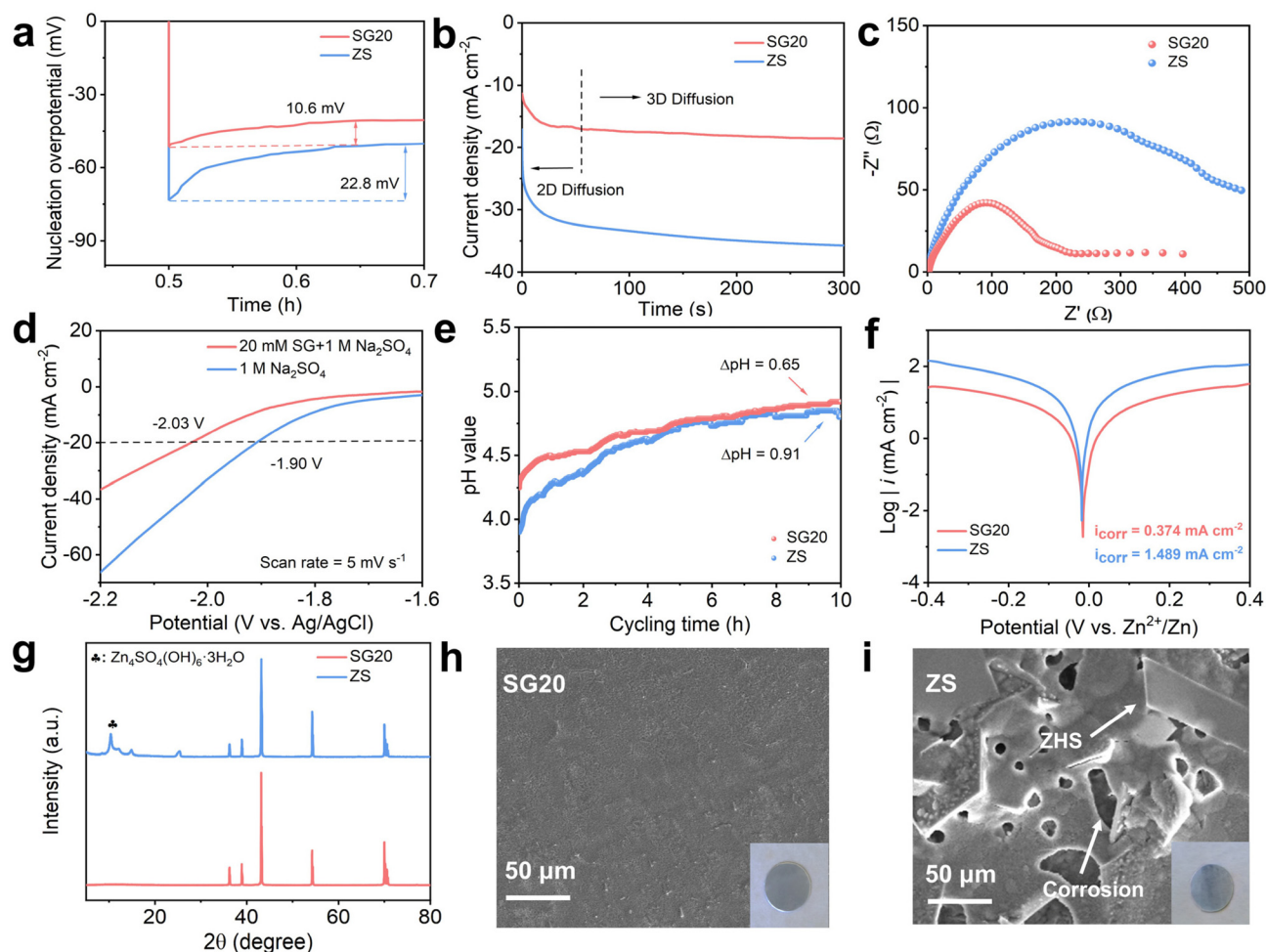
Fig. 4 (a) Initial Zn nucleation overpotential of Zn||Cu asymmetric cells using SG20 and ZS electrolytes at 1 mA cm^{-2}. (b) CA curves of Zn||Zn symmetric cells using SG20 and ZS electrolytes at a constant overpotential of −200 mV. (c) EIS plots of Zn||Zn symmetric cells assembled using SG20 and ZS electrolytes. (d) LSV curves of Zn||Zn symmetrical cells using 1 M Na_2SO_4 electrolyte and 20 mM SG in 1 M Na_2SO_4 electrolyte at a scan rate of 5 mV s^{-1}. (e) *In situ* pH tests of SG20 and ZS electrolytes during cycling. (f) Tafel plots of Zn electrodes obtained in SG20 and ZS electrolytes. (g) XRD patterns of Zn anodes after being soaked in SG20 and ZS electrolytes for three days. SEM images of the Zn anodes after soaking tests in (h) SG20 and (i) ZS electrolytes.

of the HER activity of the Zn electrode in the SG20 electrolyte. Furthermore, *in situ* pH tests were conducted to monitor the pH changes of the electrolytes during Zn plating/stripping. As shown in Fig. 4e, the SG20 electrolyte showed an initial pH of 4.25, slightly higher than that (3.9) of the ZS electrolyte due to the weak alkalinity of SG molecules.[30,31] Notably, compared to that of the ZS electrolyte, the pH of the SG20 electrolyte increased more slowly during Zn plating/stripping, agreeing well with the suppressed HER activity of the Zn electrode in the SG20 electrolyte.

Tafel tests were conducted to investigate the corrosion behaviors of the Zn electrodes in different electrolytes, as shown in Fig. 4f. The corrosion current density decreased from 1.5 mA cm^{-2} in the ZS electrolyte to 0.4 mA cm^{-2} in the SG20 electrolyte, implying effectively suppressed Zn corrosion in the presence of SG molecules. To further evaluate the anti-corrosion performance, the Zn electrodes were immersed in SG20

and ZS electrolytes for 3 days (Fig. S8†). As shown in Fig. 4g and Fig. S9,† new diffraction peaks corresponding to ZHS appeared for the Zn electrode immersed in the ZS electrolyte. In contrast, these peaks were not observed for the Zn electrode soaked in the SG20 electrolyte. As displayed in Fig. 4h, the surface of the Zn electrode immersed in the SG20 electrolyte remained a smooth metallic surface and no ZHS flakes could be identified. However, the Zn electrode immersed in the ZS electrolyte suffered from severe pitting corrosion and ZHS passivation (Fig. 4i) because of side reactions. These findings strongly supported that SG molecules not only inhibited Zn dendrite growth but also alleviated water-induced side reactions at the Zn/electrolyte interface.

To investigate the effect of the SG additive in practical applications, $NH_4V_4O_{10}$ was employed as the cathode material to assemble full cells. Fig. S10† shows the XRD pattern of the synthesized $NH_4V_4O_{10}$, which is consistent with the results
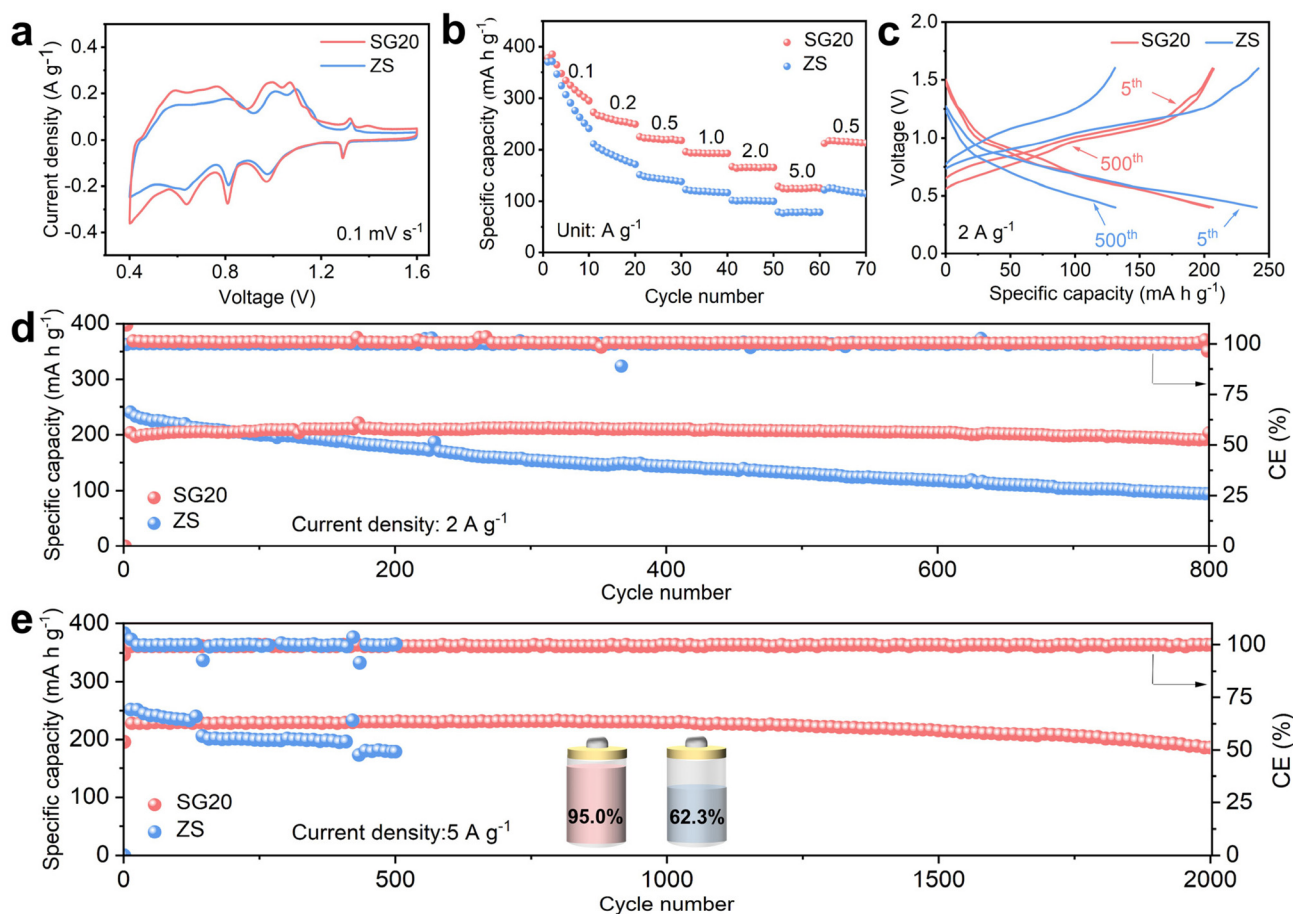
Fig. 5 (a) CV plots of $NH_4V_4O_{10}$||Zn full cells using SG20 and ZS electrolytes at a scan rate of 0.1 mV s^{-1}. (b) Rate performance of $NH_4V_4O_{10}$||Zn full cells using SG20 and ZS electrolytes. (c) Voltage profiles and (d) long-term cycling performance of $NH_4V_4O_{10}$||Zn full cells at a current density of 2 A g^{-1}. (e) Long-term cycling performance of $NH_4V_4O_{10}$||Zn full cells at a current density of 5 A g^{-1}.

reported in our prior work.[32,33] As shown in Fig. 5a, the cyclic voltammetry curves of the $NH_4V_4O_{10}$||Zn full cells with ZS and SG20 electrolytes displayed similar reduction/oxidation peaks. This indicated that SG molecules were chemically stable and remained effective during charge/discharge.[34,35] Fig. 5b depicts the rate performance of the full cells at current densities ranging from 0.1 to 5 A g^{-1}. The full cells based on SG20 and ZS electrolytes possessed similar initial capacities at a current density of 0.1 A g^{-1}. However, in the subsequent cycles, the SG20-based full cell exhibited higher discharge capacities during the rate tests, indicating its excellent rate capability. Moreover, the SG20-based full cell exhibited a smaller R_{ct} than the ZS-based full cell (Fig. S11†), consistent with the phenomena observed in symmetric cells, as shown in Fig. 4c.

Fig. 5c shows the charge/discharge curves of the SG20-based $NH_4V_4O_{10}$||Zn full cell at a current density of 2 A g^{-1}. The voltage profiles and capacities of the SG20-based $NH_4V_4O_{10}$||Zn full cell remained nearly unchanged over 500 cycles, indicating its excellent long-term cycling stability. Comparatively, the ZS-based full cell exhibited fast capacity

degradation due to increased polarization during cycling. Fig. 5d shows the long-term cycling stability of these full cells at 2 A g^{-1}. Notably, the SG20-based full cell retained 94.3% of its initial capacity after 800 cycles with a high average CE of approximately 100%. Meanwhile, the capacity of the ZS-based full cell rapidly decayed to 31% of its initial value due to severe water-induced side reactions occurring at the Zn/electrolyte interface. Fig. 5e displays the long-term cycling performance of the full cells at a higher current density of 5 A g^{-1}. During cycling, the ZS-based full cell experienced fast capacity degradation and quick failure after approximately 200 cycles because of Zn dendrite growth. In sharp contrast, the SG20-based full cell demonstrated excellent cycling stability with a high capacity retention rate of 95% after 2000 cycles, equivalent to only a 0.005 mA h g^{-1} decay per cycle (Fig. S12†). As shown in Fig. S13,† the voltage profiles of the SG20-based $NH_4V_4O_{10}$||Zn full cell at 5 A g^{-1} remained nearly unchanged over 1000 cycles. These results corroborate that the SG additive can effectively stabilize the Zn anode by inhibiting Zn dendrite growth and side reactions, resulting in enhanced electrochemical performance of AZIBs.

3. Conclusion

In summary, SG is an efficient and effective electrolyte additive to inhibit Zn dendrite growth and side reactions for achieving high-performance AZIBs. Theoretical calculations and experiments together confirm that SG molecules are preferentially absorbed on the Zn (101) and (100) planes. Meanwhile, the Zn (002) plane can be exposed to Zn^{2+}, enabling the planar growth of Zn deposits during cycling. Furthermore, the presence of SG molecules effectively alleviates side reactions at the Zn/electrolyte interface. Consequently, the Zn||Zn symmetric cell with the SG electrolyte additive exhibits excellent cycling stability over 2000 h at 1 mA cm^{-2} and 1 mA h cm^{-2}. Even at a high current density of 5 mA cm^{-2} and a high areal capacity of 2.5 mA h cm^{-2}, the SG20-based symmetric cell shows superior cycling stability over 900 h. More importantly, the $NH_4V_4O_{10}$|| Zn full cell with the SG20 electrolyte shows a high capacity retention rate of 95% over 2000 cycles at a current density of 5 A g^{-1}. The low-cost SG electrolyte additive presents a promising strategy for improving the performance and durability of AZIBs.

Conflicts of interest

The authors declare no conflict of interest.

Acknowledgements

References

1 J. Li, Z. Liu, S. Han, P. Zhou, B. Lu, Z. Zeng, Z. Chen and J. Zhou, *Nano-Micro Lett.*, 2023, **15**, 237.

2 X. Xie, J. Li, Z. Xing, B. Lu, S. Liang and J. Zhou, *Natl. Sci. Rev.*, 2023, **10**, nwac281.

3 F. Schipper and D. Aurbach, *Russ. J. Electrochem.*, 2016, **52**, 1095–1121.

4 T. Kim, W. Song, D.-Y. Son, L. K. Ono and Y. Qi, *J. Mater. Chem. A*, 2019, **7**, 2942–2964.

5 P. Ruan, S. Liang, B. Lu, H. J. Fan and J. Zhou, *Angew. Chem.*, 2022, **134**, e202200598.

6 Z. Liu, L. Qin, B. Lu, X. Wu, S. Liang and J. Zhou, *ChemSusChem*, 2022, **15**, e202200348.

7 B. Tang, L. Shan, S. Liang and J. Zhou, *Energy Environ. Sci.*, 2019, **12**, 3288–3304.

8 P. Ruan, X. Xu, D. Zheng, X. Chen, X. Yin, S. Liang, X. Wu, W. Shi, X. Cao and J. Zhou, *ChemSusChem*, 2022, **15**, e202201118.

9 B. Li, X. Zhang, T. Wang, Z. He, B. Lu, S. Liang and J. Zhou, *Nano-Micro Lett.*, 2022, **14**, 6.

10 Q. Zhang, Y. Ma, Y. Lu, X. Zhou, L. Lin, L. Li, Z. Yan, Q. Zhao, K. Zhang and J. Chen, *Angew. Chem., Int. Ed.*, 2021, **60**, 23357–23364.

11 L. Wang, W. Huang, W. Guo, Z. H. Guo, C. Chang, L. Gao and X. Pu, *Adv. Funct. Mater.*, 2022, **32**, 2108533.

12 S.-B. Wang, Q. Ran, R.-Q. Yao, H. Shi, Z. Wen, M. Zhao, X.-Y. Lang and Q. Jiang, *Nat. Commun.*, 2020, **11**, 1634.

13 Z. Xing, Y. Sun, X. Xie, Y. Tang, G. Xu, B. Lu, J. Han, S. Liang, G. Chen and J. Zhou, *Angew. Chem., Int. Ed.*, 2023, **62**, e202215324.

14 C. Deng, X. Xie, J. Han, B. Lu, S. Liang and J. Zhou, *Adv. Funct. Mater.*, 2021, **31**, 2103227.

15 C. Peng, Y. Zhang, S. Yang, L.-L. Zhang and Z. Wang, *Nano Energy*, 2022, **98**, 107329.

16 Y. Song, P. Ruan, C. Mao, Y. Chang, L. Wang, L. Dai, P. Zhou, B. Lu, J. Zhou and Z. He, *Nano-Micro Lett.*, 2022, **14**, 218.

17 J. Liu, W. Song, Y. Wang, S. Wang, T. Zhang, Y. Cao, S. Zhang, C. Xu, Y. Shi, J. Niu and F. Wang, *J. Mater. Chem. A*, 2022, **10**, 20779–20786.

18 J. Hao, L. Yuan, C. Ye, D. Chao, K. Davey, Z. Guo and S.-Z. Qiao, *Angew. Chem., Int. Ed.*, 2021, **60**, 7366–7375.

19 N. Wang, X. Chen, H. Wan, B. Zhang, K. Guan, J. Yao, J. Ji, J. Li, Y. Gan, L. Lv, L. Tao, G. Ma, H. Wang, J. Zhang and H. Wang, *Adv. Funct. Mater.*, 2023, **33**, 2300795.

20 W. Zhang, Y. Dai, R. Chen, Z. Xu, J. Li, W. Zong, H. Li, Z. Li, Z. Zhang, J. Zhu, F. Guo, X. Gao, Z. Du, J. Chen, T. Wang, G. He and I. Parkin, *Angew. Chem.*, 2023, **135**, e202212695.

21 Z. Hu, F. Zhang, Y. Zhao, H. Wang, Y. Huang, F. Wu, R. Chen and L. Li, *Adv. Mater.*, 2022, **34**, 2203104.

22 C. Meng, W. He, L. Jiang, Y. Huang, J. Zhang, H. Liu and J.-J. Wang, *Adv. Funct. Mater.*, 2022, **32**, 2207732.

23 H. Zhang, Y. Zhong, J. Li, Y. Liao, J. Zeng, Y. Shen, L. Yuan, Z. Li and Y. Huang, *Adv. Energy Mater.*, 2023, **13**, 2203254.

24 K. E. K. Sun, T. K. A. Hoang, T. N. L. Doan, Y. Yu, X. Zhu, Y. Tian and P. Chen, *ACS Appl. Mater. Interfaces*, 2017, **9**, 9681–9687.

25 Y. Wang, S. Zhang, H. Wang, Y. Wang, Y. Liu, S. Dou, X. Miao, W. Deng, X. Lin and Q. Yuan, *J. Mater. Chem. A*, 2023, **11**, 17207–17216.

26 M. Zhou, S. Guo, J. Li, X. Luo, Z. Liu, T. Zhang, X. Cao, M. Long, B. Lu, A. Pan, G. Fang, J. Zhou and S. Liang, *Adv. Mater.*, 2021, **33**, 2100187.

27 T. C. Li, Y. Lim, X. L. Li, S. Luo, C. Lin, D. Fang, S. Xia, Y. Wang and H. Y. Yang, *Adv. Energy Mater.*, 2022, **12**, 2103231.

28 A. Pei, G. Zheng, F. Shi, Y. Li and Y. Cui, *Nano Lett.*, 2017, **17**, 1132–1139.

29 Y. Lin, Z. Mai, H. Liang, Y. Li, G. Yang and C. Wang, *Energy Environ. Sci.*, 2023, **16**, 687–697.

30 M. Zhang, H. Hua, P. Dai, Z. He, L. Han, P. Tang, J. Yang, P. Lin, Y. Zhang, D. Zhan, J. Chen, Y. Qiao, C. C. Li, J. Zhao and Y. Yang, *Adv. Mater.*, 2023, **35**, 2208630.

31 R. E. Shetlar and D. W. Towle, *Am. J. Physiol.: Regul., Integr. Comp. Physiol.*, 1989, **257**, R924–R931.

32 P. Wang, S. Liang, C. Chen, X. Xie, J. Chen, Z. Liu, Y. Tang, B. Lu and J. Zhou, *Adv. Mater.*, 2022, **34**, 2202733.

33 Y. Liu, S. Liu, X. Xie, Z. Li, P. Wang, B. Lu, S. Liang, Y. Tang and J. Zhou, *InfoMat*, 2023, **5**, e12374.

34 S. Tian, L. Zhou, W. He, Y. Tian, Y. Zhou, S. Wu, R. Jian, K. J. Balkus, T. Luo and G. Xiong, *Chem. Eng. J.*, 2023, **462**, 142276.

35 S. Tian, T. Hwang, Y. Tian, Y. Zhou, L. Zhou, T. Milazzo, S. Moon, S. Malakpour Estalaki, S. Wu, R. Jian, K. Balkus, T. Luo, K. Cho and G. Xiong, *ACS Nano*, 2023, **17**, 14930–14942.